 CMES, vol.44, no.1, pp.1-34, 2009

Large Deformation Applications with the Radial Natural Neighbours Interpolators

L.M.J.S. Dinis[1], **R.M. Natal Jorge**[2] **and J. Belinha**[3]

Abstract: The Natural Neighbour Radial Point Interpolation Method (NNRPIM) is extended to the large deformation analysis of non-linear elastic structures. The nodal connectivity in the NNRPIM is enforced using the Natural Neighbour concept. After the Voronoï diagram construction of the unstructured nodal mesh, which discretize the problem domain, small cells are created, the "influence-cells". These cells are in fact influence-domains entirely nodal dependent. The Delaunay triangles are used to create a node-depending background mesh used in the numerical integration of the NNRPIM interpolation functions. The NNRPIM interpolation functions, used in the Galerkin weak form, are constructed with the Radial Point Interpolators. In the construction of the NNRPIM interpolation functions no polynomial base is required, which is an innovation and the used Radial Basis Function (RBF) is the Multiquadric RBF. The NNRPIM interpolation functions posses the delta Kronecker property, which simplify the imposition of the natural and essential boundary conditions. Once the scope of this work is to extend and validate the NNRPIM in the large-deformation analysis, the used non-linear solution algorithm is the Orthogonal Actualized Ramm's method, which permits the analysis of structures that in some point evidence instability phenomenons such as the "snap-through" and the "snap-back". Several non-linear benchmark examples are studied to demonstrate the effectiveness of the method. The numerical results indicated that NNRPIM handles large material distortion effectively and provides an accurate solution under large deformation.

Keywords: Radial Point Interpolation Method (RPIM), Radial Basis Function (RBF), Natural Neighbours, Meshfree Method, Large Deformations, Non-Linear.

[1] FEUP, Porto, Portugal - e-mail: ldinis@fe.up.pt
[2] FEUP, Porto, Portugal - e-mail: rnatal@fe.up.pt
[3] IDMEC, Porto, Portugal - e-mail: jorge.belinha@fe.up.pt

1 Introduction

Meshless methods [Belytschko T., Krongauz Y. et al., (1996); Gu Y.T., (2005)] were created and developed in order to answer to some drawbacks and limitations found in the Finite Element Method (FEM). Since the field functions are approximated within a flexible influence domain rather an element, in the meshless methods the nodes can be randomly distributed. In opposition to the no-overlap rule between elements in the FEM, in meshless methods the influence domains may and must overlap each other.

Meshless methods can be classified in two categories, a first category that pursue the weak form solution and another that seek the strong form solution. In the first category the meshless methods can be once more divided, the ones that use approximation functions [Monaghan J.J., (1977); Lancaster P. and Salkauskas K., (1981); Nayroles B., Touzot G. et al., (1992); Belytschko T., Lu Y.Y. et al., (1994); Lu Y., Belytschko T. et al., (1994); Liu W.K., Jun S. et al., (1995); Atluri S.N. and Zhu T., (1998); Atluri S.N. and Shen S., (2002); Sladek V., Sladek J. et al., (2003); Vavourakis V., Sellountos E.J. et al., (2006)] and others that use interpolation functions. Meshless methods based in approximation functions have been successfully applied in computational mechanics [Long S. and Atluri S.N, (2002); Qian L.F., Batra R.C. et al., (2003); Sori J., Q. Li Q. et al., (2004); Han Z.D., Rajendran A.M. et al., (2005); Wen P.H. and Hon Y.C., (2007); Juan Z., Shuyao L. et al., (2008); Mohammadi M.H., (2008)], and even its difficulty on imposing the essential and natural boundary conditions has been overcome with the use of efficient numerical methods. This original difficulty is due to the lack of the delta Kronecker property, $\varphi_i(x_j) \neq \delta_{ij}$, which is an immediate consequence of using approximation functions instead of interpolation functions.

At the time, to address the above problem, several meshless methods, using interpolation functions, were developed. Such as the Point Interpolation Method (PIM) [Liu G.R. and Gu Y.T., (2001)], the Point Assembly Method [Liu G.R., (2002b)], Radial Point Interpolation Method (RPIM) [Wang J.G. and Liu G.R., (2002b)], the Meshless Local Natural Neighbour Interpolation Method (MLNNIM) [Liu Y.H., Chen S.S. et al., (2008)], the Generalized Interpolation Material Point Method (GIMPM) [Bardenhagen S.G. and Kober E.M., (2004); Ma J., Lu H. et al., (2006)] and the Natural Neighbour Finite Elements Methods (NNFEM) [Traversoni L., (1994); Sukumar N., Moran B. et al., (2001); Atluri S.N., Han Z.D. et al., (2004)] or Natural Element Method (NEM) [Braun J. and Sambridge M., (1995); Sukumar N., Moran B. et al., (1998); Cueto E., Doblaré M. et al., (2000); Cueto E., Sukumar N. et al., (2003)].

Recently an improved meshless method was developed, the Natural Neighbour Radial Point Interpolation Method (NNRPIM) [Dinis L., Jorge R.N. et al., (2007a); Dinis L., Jorge R.N. et al., (2007b); Dinis L., Jorge R.N. et al., (2008)]. The NNRPIM uses mathematic concepts, such as Voronoï Diagrams [Voronoï G.M., (1908)] and the Delaunay tessellation [Delaunay B., (1934)], to construct the influence-cells, the basic structure of the nodal connectivity in the NNRPIM, and the background integration mesh, totally dependent on the nodal mesh. Unlike the FEM, where geometrical restrictions on elements are imposed for the convergence of the method, in the NNRPIM there are no such restrictions, which permits a random node distribution for the discretized problem. The NNRPIM interpolation functions, used in the Galerkin weak form, are constructed with the Radial Point Interpolators (RPI). The NNRPIM interpolation functions possess the delta Kronecker property and its construction is simple and its derivatives are easily obtained. The radial basis function (RBF) used in the RPI is the multiquadric RBF. The RBF was firstly used for data surface fitting, and later, with the work developed by Kansa [Kansa E.J., (1990); Devi K.N. and Pepper D.W., (2004); Leevan Ling, (2005)] the RBF was used for solving partial differential equations. However the NNRPIM uses, unlike Kansa's algorithm, the concept of "influence domain" instead of "global domain", generating sparse and banded stiffness matrices, more convenient to complex geometry problems.

This paper is organized as follows: In section 2 the NNRPIM is presented, the creation of the influence-cells, the used integration scheme and the construction of the interpolation functions are summarized. In section 3 the large deformation formulation adapted to the NNRPIM is presented. In section 4 the NNRPIM is implemented, several well-known benchmark examples are solved. This paper ends with the conclusions and remarks in section 5.

2 Radial Natural Neighbour Interpolators

The NNRPIM uses the Voronoï diagrams and the Delaunay triangulation, which are useful mathematical tools, in the determination of the natural neighbours [Sibson R., (1980)] for each node belonging to the global nodal set $\mathbf{N} = \{n_1, n_2, \dots, n_N\} \in IR^3$. This theory is applicable to a IN dimensional space. The Voronoï diagram of $\mathbf{N}$ is the partition of the domain defined by $\mathbf{N}$ in sub-regions V_I, closed and convex. Each sub-region V_I is associated with the node I, n_I, in a way that any point in the interior of the V_I is closer to n_I than any other node n_J, where $n_J \in \mathbf{N}\,(J \neq I)$, figure 1(a). The sub-regions V_K are defined as "Voronoï cells" which form the Voronoï diagram, $k = 1, \dots, N$.

2.1 Nodal Connectivity

The nodal connectivity is imposed by the overlap of the influence-cells [Dinis L., Jorge R.N. et al., (2007a)], similar to the influence domain concept, which are obtained from the Voronoï cells. The cell formed by n nodes that contributes to the interpolation of the interest point $\mathbf{x}_I$ is called "influence-cell". Two distinct types of influence-cells are presented in figure 1(b).

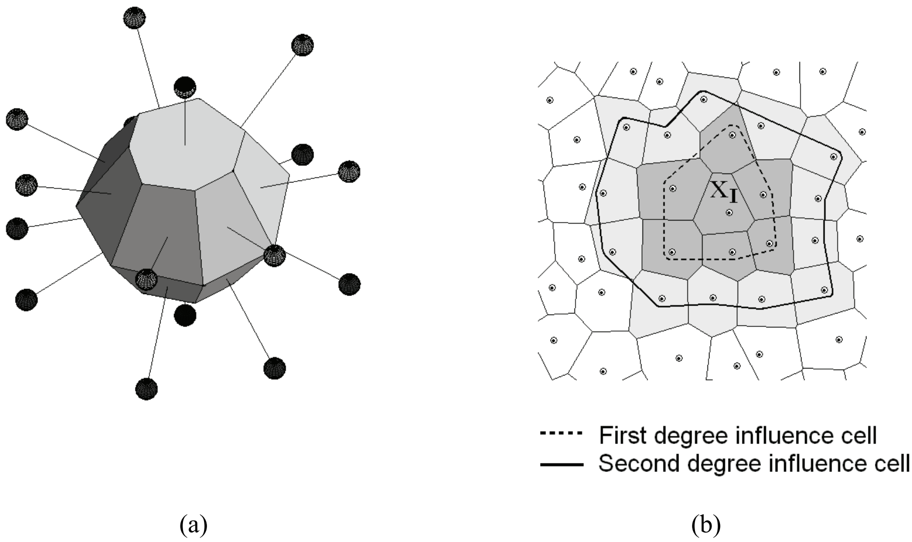

Figure 1: (a) 3D Voronoï cell. (b) Influence cells representation.

First degree influence-cell: A point of interest, $\mathbf{x}_I$ searches for its neighbour nodes following the Natural Neighbour Voronoï construction. Thus the *first degree influence-cell* is composed by these first natural neighbours.

Second degree influence-cell: A point of interest, $\mathbf{x}_I$ searches for its neighbour nodes, in the same manner as in the *first degree influence-cell*. Then, based on a previous construction of the Voronoï diagram for the node mesh, the natural neighbours of the first natural neighbours of $\mathbf{x}_I$ are added to the influence-cell.

2.2 Numerical Integration

In an initial phase, after the domain discretization in a regular or an irregular nodal mesh, the Voronoï cells of each node are constructed. These cells can be considered as a background mesh for integration purpose, being determined the influence-cell for each one of these integration points. Using the Voronoï tessellation and the

Delaunay triangulation small areas or volumes, respectively for the 2-Dimensional case and for the 3-Dimensional case, are established, figure 2(a). These areas or volumes, 2(b), can be isoparameterized and the Gauss-Legendre quadrature scheme applied, 2(c). In this work the Gauss-Legendre quadrature scheme was used: 1x1 for 2-Dimensional cases; 1x1x1 for 3-Dimensional cases. These two integrations schemes are sufficient for the used NNRPIM formulation [Dinis L., Jorge R.N. et al., (2007a)].

2.3 Radial Point Interpolators

It was found in previous works on the NNRPIM [Dinis L., Jorge R.N. et al., (2007a); Dinis L., Jorge R.N. et al., (2007b); Dinis L., Jorge R.N. et al., (2008)] that the polynomial basis of the classic Radial Point Interpolators (RPIs) is unnecessary if the shape parameters of the radial basis function (RBF) are chosen carefully. Thus, consider a function $\mathbf{u}(\mathbf{x})$ defined in the domain Ω, which is discretized by a set of N nodes. In the NNRPIM the function $\mathbf{u}(\mathbf{x})$ passes through all nodes using a radial basis function. It is assumed that only the nodes within the influence-cell of the point of interest $\mathbf{x}_I$ have effect on $\mathbf{u}(\mathbf{x}_I)$. The value of function $\mathbf{u}(\mathbf{x}_I)$ at the point of interest x_I is obtained by,

$$\mathbf{u}(\mathbf{x}_I) = \sum_{i=1}^{n} R_i(\mathbf{x}_I)\; a_i(\mathbf{x}_I) = \mathbf{R}(\mathbf{x}_I)\,\mathbf{a}(\mathbf{x}_I) \tag{1}$$

where $R_i(\mathbf{x}_I)$ is the RBF, n is the number of nodes inside the influence-cell of $\mathbf{x}_I$. The coefficients $a_i(\mathbf{x}_I)$ are non constant coefficients of $R_i(\mathbf{x}_I)$.

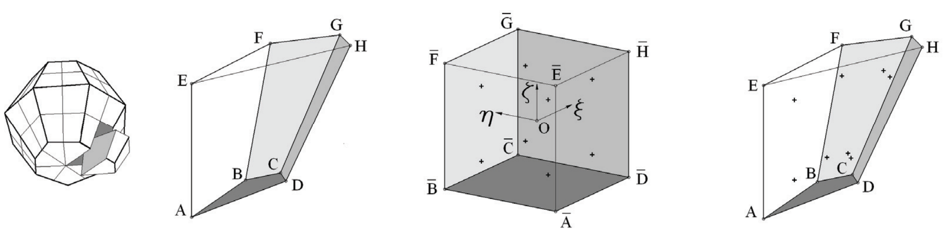

(a) (b) (c) (d)

Figure 2: (a) Voronoï cell and respective tetrahedrons. (b) Initial tetrahedron. (c) Initial tetrahedron isoparameterization and determination of the quadrature integration points. (d) Quadrature integration points in Cartesians coordinates.

In the RBF the variable is the distance r_{Ii} between the relevant node $\mathbf{x}_I$ and the neighbour node $\mathbf{x}_i$, $r_{Ii} = \sqrt{(x_I - x_i)^2 + (y_I - y_i)^2 + (z_I - z_i)^2}$. Several known RBFs are well studied and developed in [Wang J.G. and Liu G.R., (2002b)] The present work uses the Multiquadric (MQ) function proposed initially by Hardy [Hardy R.L., (1990)].

$$R(r_{Ii}) = \left(r_{Ii}^2 + c^2\right)^p \tag{2}$$

where c and p are two shape parameters. The optimized values of c and p can be found in [Dinis L., Jorge R.N. et al., (2007a); Dinis L., Jorge R.N. et al., (2007b)]. Equation (1) can be written in the matricial form,

$$\mathbf{u}_s = \mathbf{R}_G\,\mathbf{a} \tag{3}$$

And solved by substitution on equation (1),

$$\mathbf{u}(\mathbf{x}_I) = \mathbf{R}(\mathbf{x}_I)\,\mathbf{R}_G^{-1}\,\mathbf{u}_s = \varphi(\mathbf{x}_I)\,\mathbf{u}_s \tag{4}$$

where $\varphi(\mathbf{x}_I)$ is the interpolation function defined as,

$$\varphi(\mathbf{x}_I) = R(\mathbf{x}_I)\,\mathbf{R}_G^{-1} = \begin{pmatrix}\varphi_1(\mathbf{x}_I) & \varphi_2(\mathbf{x}_I) & \dots & \varphi_n(\mathbf{x}_I)\end{pmatrix} \tag{5}$$

The partial derivative of $\varphi(\mathbf{x}_I)$ is easily obtained [Dinis L., Jorge R.N. et al., (2007a)]. Early works on the RPIM [Wang J.G. and Liu G.R., (2002b); Wang J.G. and Liu G.R., (2002a)] sustain that these interpolation functions possess the delta Kronecker property and also that the partition of unity is satisfied. An inconvenient property of the RPIMs interpolation functions is the lack of compatibility. This property is achieved in the RPIMs using the conforming RPIM [Liu G.R., Gu Y.T. et al., (2004)]. However this same study concluded that the RPIM is much more simple and efficient than the conforming RPIM. The lack of consistency in the RPIMs interpolation functions, constructed without a polynomial basis, is the reason why this formulation cannot pass the standard path test, although it is proved that it can approach polynomials in the desired accuracy and the convergence is guaranteed when the nodes are refined [Liu G.R., (2002a)].

3 Large Deformation Formulation

3.1 Non-linear solid mechanics

In a large deformation analysis a body can experience a large rotation and/or a large strain. The defined stress terms together with the obtained strain terms make it possible to express the virtual work as an integral over the known body volume, expressing in this manner the change in the body configuration. Both strain tensor and stress tensor are referred to the same deformed state. The Cauchy stress tensor, defined as $\mathbf{\Lambda}$, is a symmetric tensor and it represents the stresses of the current configuration, for the three-dimensional case it can be defined as,

$$\mathbf{\Lambda} = \begin{bmatrix} \sigma_{xx} & \tau_{zx} & \tau_{yz} \\ \tau_{zx} & \sigma_{yy} & \tau_{xy} \\ \tau_{yz} & \tau_{xy} & \sigma_{zz} \end{bmatrix} \tag{6}$$

In this work it is used the Voigt notation, since the development of fourth order tensors is less practical. In Voigt notation the second order term tensors are expressed in column vectors, so the stress tensor $\mathbf{\Lambda}$ is reduced to the stress vector $\boldsymbol{\sigma}$,

$$\boldsymbol{\sigma} = \left\{ \sigma_{xx} \quad \sigma_{yy} \quad \sigma_{zz} \quad \tau_{xy} \quad \tau_{yz} \quad \tau_{zx} \right\}^T \tag{7}$$

And the strain tensor $\mathbf{E}$ to the strain vector $\boldsymbol{\varepsilon}$,

$$\boldsymbol{\varepsilon} = \left\{ \varepsilon_{xx} \quad \varepsilon_{yy} \quad \varepsilon_{zz} \quad \varepsilon_{xy} \quad \varepsilon_{yz} \quad \varepsilon_{zx} \right\}^T \tag{8}$$

The strain tensor $\mathbf{E}$ is defined by,

$$\mathbf{E} = \frac{1}{2}\left(\mathbf{C} - \mathbf{I}\right) \tag{9}$$

being $\mathbf{I}$ the identity matrix and $\mathbf{C}$ the right Cauchy-Green deformation tensor,

$$\mathbf{C} = \mathbf{F}^T \mathbf{F} \tag{10}$$

where $\mathbf{F}$ is the deformation gradient which can be written as,

$$\mathbf{F} = \frac{\partial \mathbf{x}}{\partial \mathbf{X}} \tag{11}$$

being the body initial material position represented as $\mathbf{X} = \{X \ Y \ Z\}$ and the body current material position represented as $\mathbf{x} = \{x \, y \, z\}$.
The following relation between the stress rate and the strain rate is assumed,

$$d\boldsymbol{\sigma} = \mathbf{c} \, d\boldsymbol{\varepsilon} \tag{12}$$

The material matrix is defined by $\mathbf{c}$ and if material non-linear relations exists between $\boldsymbol{\sigma}$ and $\boldsymbol{\varepsilon}$, then $\mathbf{c} = \mathbf{c}^{eP}$. For the three-dimensional elasticity case,

$$\mathbf{c} = \mu_1 \begin{bmatrix} 1 & \nu & \nu & 0 & 0 & 0 \\ \nu & 1 & \nu & 0 & 0 & 0 \\ \nu & \nu & 1 & 0 & 0 & 0 \\ 0 & 0 & 0 & \mu_2 & 0 & 0 \\ 0 & 0 & 0 & 0 & \mu_2 & 0 \\ 0 & 0 & 0 & 0 & 0 & \mu_2 \end{bmatrix} \tag{13}$$

being $\mu_1 = E/(1-\nu^2)$ and $\mu_2 = (1-\nu)/2$, where E is the Young Modulus and ν is Poisson ratio. The NNRPIM formulation is established in terms of a weak form of the differential equation under consideration. In the solid mechanics context this implies the use of the virtual work equation,

$$\psi = \int_\Omega \boldsymbol{\sigma}\, d\boldsymbol{\varepsilon}\, d\Omega - \int_\Omega \mathbf{b}\cdot d\mathbf{u}\, d\Omega - \int_\Gamma \mathbf{t}\cdot d\mathbf{u}\, d\Gamma = 0 \tag{14}$$

where $\mathbf{b}$ is the body force and $\mathbf{t}$ is the surface force, respectively acting on the solid volume Ω and surface Γ, both in the current configuration. The virtual displacement is defined by $d\mathbf{u}$ and $d\boldsymbol{\varepsilon}$ is defined by,

$$d\boldsymbol{\varepsilon} = \bar{\mathbf{B}}\, d\mathbf{u} \tag{15}$$

where $\mathbf{u} = \{u\ v\ w\}$ displacement and $\bar{\mathbf{B}}$ is the deformation matrix. Thus the virtual work, expressed in equation (14), using equation (15) can be presented as,

$$\psi = \int_\Omega \bar{\mathbf{B}}^T \boldsymbol{\sigma}\, d\Omega - \mathbf{f} = 0 \tag{16}$$

being $\mathbf{f}$ the applied total force vector. The strain vector can be divided in two parts, the linear part and the non-linear part,

$$\boldsymbol{\varepsilon} = \boldsymbol{\varepsilon}_0 + \boldsymbol{\varepsilon}_{NL} \tag{17}$$

which can also be presented as,

$$\boldsymbol{\varepsilon} = \underbrace{\mathbf{L}\boldsymbol{\theta}}_{\boldsymbol{\varepsilon}_0} + \underbrace{\tfrac{1}{2}\mathbf{A}\boldsymbol{\theta}}_{\varepsilon_{NL}} = \left(\mathbf{L} + \tfrac{1}{2}\mathbf{A}\right)\boldsymbol{\theta} \tag{18}$$

The matrix $\mathbf{L}$ is defined as,

$$\mathbf{L} = \begin{bmatrix} \mathbf{e}_1 & \underset{[3\times1]}{\mathbf{0}} & \underset{[3\times1]}{\mathbf{0}} & \mathbf{e}_2 & \underset{[3\times1]}{\mathbf{0}} & \mathbf{e}_3 \\ \underset{[3\times1]}{\mathbf{0}} & \mathbf{e}_2 & \underset{[3\times1]}{\mathbf{0}} & \mathbf{e}_1 & \mathbf{e}_3 & \underset{[3\times1]}{\mathbf{0}} \\ \underset{[3\times1]}{\mathbf{0}} & \underset{[3\times1]}{\mathbf{0}} & \mathbf{e}_3 & \underset{[3\times1]}{\mathbf{0}} & \mathbf{e}_2 & \mathbf{e}_1 \end{bmatrix}^T \tag{19}$$

Being $\mathbf{e}_i$ the coordinate i director column vector,

$$\mathbf{I} = \begin{bmatrix} \mathbf{e}_1 & \mathbf{e}_2 & \mathbf{e}_3 \end{bmatrix} \tag{20}$$

The column vector $\boldsymbol{\theta}$ is defined by,

$$\boldsymbol{\theta} = \mathbf{G}\,\mathbf{u} \tag{21}$$

Being $\mathbf{G}$ the geometric matrix defined by,

$$\mathbf{G}^T = \begin{bmatrix} \frac{\partial\varphi}{\partial x} & 0 & 0 & \frac{\partial\varphi}{\partial y} & 0 & 0 & \frac{\partial\varphi}{\partial z} & 0 & 0 \\ 0 & \frac{\partial\varphi}{\partial x} & 0 & 0 & \frac{\partial\varphi}{\partial y} & 0 & 0 & \frac{\partial\varphi}{\partial z} & 0 \\ 0 & 0 & \frac{\partial\varphi}{\partial x} & 0 & 0 & \frac{\partial\varphi}{\partial y} & 0 & 0 & \frac{\partial\varphi}{\partial z} \end{bmatrix} \tag{22}$$

which produces the following column vector $\boldsymbol{\theta}$,

$$\boldsymbol{\theta} = \begin{bmatrix} \boldsymbol{\theta}_x^T & \boldsymbol{\theta}_y^T & \boldsymbol{\theta}_z^T \end{bmatrix}^T \text{ being } \boldsymbol{\theta}_\xi = \begin{bmatrix} \frac{\partial u}{\partial \xi} & \frac{\partial v}{\partial \xi} & \frac{\partial w}{\partial \xi} \end{bmatrix}^T \tag{23}$$

The current configuration displacement is considered in matrix $\mathbf{A}$, the equation (18) actualized component,

$$\mathbf{A} = \begin{bmatrix} \boldsymbol{\theta}_x & \underset{[3\times1]}{\mathbf{0}} & \underset{[3\times1]}{\mathbf{0}} & \boldsymbol{\theta}_y & \underset{[3\times1]}{\mathbf{0}} & \boldsymbol{\theta}_z \\ \underset{[3\times1]}{\mathbf{0}} & \boldsymbol{\theta}_y & \underset{[3\times1]}{\mathbf{0}} & \boldsymbol{\theta}_x & \boldsymbol{\theta}_z & \underset{[3\times1]}{\mathbf{0}} \\ \underset{[3\times1]}{\mathbf{0}} & \underset{[3\times1]}{\mathbf{0}} & \boldsymbol{\theta}_z & \underset{[3\times1]}{\mathbf{0}} & \boldsymbol{\theta}_y & \boldsymbol{\theta}_x \end{bmatrix}^T \tag{24}$$

The deformation matrix $\bar{\mathbf{B}}$, dependent of $\mathbf{u}$, ca be defined as,

$$\bar{\mathbf{B}} = \mathbf{B}_0 + \mathbf{B}_{NL}(\mathbf{u}) \tag{25}$$

since it varies with the deformation of the solid. The linear part of the deformation matrix is represented by $\mathbf{B}_0$ and the non-linear contribution by $\mathbf{B}_{NL}$. For the three-dimensional case,

$$\mathbf{B}_0^T = \begin{bmatrix} \frac{\partial\varphi}{\partial x} & 0 & 0 & \frac{\partial\varphi}{\partial y} & 0 & \frac{\partial\varphi}{\partial z} \\ 0 & \frac{\partial\varphi}{\partial y} & 0 & \frac{\partial\varphi}{\partial x} & \frac{\partial\varphi}{\partial z} & 0 \\ 0 & 0 & \frac{\partial\varphi}{\partial z} & 0 & \frac{\partial\varphi}{\partial y} & \frac{\partial\varphi}{\partial x} \end{bmatrix} \tag{26}$$

and

$$\mathbf{B}_{NL} = \mathbf{A}\,\mathbf{G} \tag{27}$$

The non linear deformation is actualized though matrix $\mathbf{A}$, which contains the current configuration displacements.

The tangential stiffness matrix $\mathbf{K}_T$ can be determined considering the variation of the virtual work equation, equation (16), in order to the generalized displacements $d\mathbf{u}$,

$$d\psi = d\left[\int_\Omega \bar{\mathbf{B}}^T \boldsymbol{\sigma}\, d\Omega - \mathbf{f}\right] \tag{28}$$

Considering conservative the external load, $\partial \mathbf{f}/\partial \mathbf{u} = 0$,

$$d\psi = \int_{\Omega} d\bar{\mathbf{B}}^T \boldsymbol{\sigma}\, d\Omega + \int_{\Omega} \bar{\mathbf{B}}^T d\boldsymbol{\sigma}\, d\Omega = \mathbf{K}_T\, d\mathbf{u} \tag{29}$$

Using equation (12) and equation (15) the following relation is obtained,

$$d\boldsymbol{\sigma} = \mathbf{c}\,\bar{\mathbf{B}}\, d\mathbf{u} \tag{30}$$

In the deformation matrix $\bar{\mathbf{B}}$ only the non-linear part $d\mathbf{B}_{NL}$ is dependent of $\mathbf{u}$, equation (25), thus $d\bar{\mathbf{B}} = d\mathbf{B}_{NL}$ and therefore,

$$d\psi = \int_{\Omega} d\mathbf{B}_{NL}^T \boldsymbol{\sigma}\, d\Omega + \int_{\Omega} \bar{\mathbf{B}}^T \mathbf{c}\,\bar{\mathbf{B}}\, d\Omega \tag{31}$$

where the stiffness matrix can be presented as,

$$\mathbf{K}_T = \mathbf{K}_{\sigma} + \mathbf{K}_0 + \mathbf{K}_{NL} \tag{32}$$

Being,

$$\mathbf{K}_{\sigma} = \int_{\Omega} d\mathbf{B}_{NL}^T \boldsymbol{\sigma}\, d\Omega \tag{33}$$

$$\mathbf{K}_0 = \int_{\Omega} \mathbf{B}_0^T\, \mathbf{c}\,\mathbf{B}_0\, d\Omega \tag{34}$$

$$\mathbf{K}_{NL} = \int_{\Omega} \left(\mathbf{B}_0^T\, \mathbf{c}\,\mathbf{B}_{NL} + \mathbf{B}_{NL}^T\, \mathbf{c}\,\mathbf{B}_{NL} + \mathbf{B}_{NL}^T\, \mathbf{c}\,\mathbf{B}_0 \right) d\Omega \tag{35}$$

The initial stress matrix or geometric matrix $\mathbf{K}_{\sigma}$ is defined as,

$$\mathbf{K}_{\sigma} d\mathbf{u} = \int_{\Omega} \mathbf{G}^T\, d\mathbf{A}^T\, \boldsymbol{\sigma}\, d\Omega \tag{36}$$

The variation of matrix $\mathbf{A}$ in order to $\mathbf{u}$ can be defined as,

$$d\mathbf{A}^T = \begin{bmatrix} d\boldsymbol{\theta}_x & \underset{[3\times1]}{\mathbf{0}} & \underset{[3\times1]}{\mathbf{0}} & d\boldsymbol{\theta}_y & \underset{[3\times1]}{\mathbf{0}} & d\boldsymbol{\theta}_z \\ \underset{[3\times1]}{\mathbf{0}} & d\boldsymbol{\theta}_y & \underset{[3\times1]}{\mathbf{0}} & d\boldsymbol{\theta}_x & d\boldsymbol{\theta}_z & \underset{[3\times1]}{\mathbf{0}} \\ \underset{[3\times1]}{\mathbf{0}} & \underset{[3\times1]}{\mathbf{0}} & d\boldsymbol{\theta}_z & \underset{[3\times1]}{\mathbf{0}} & d\boldsymbol{\theta}_y & d\boldsymbol{\theta}_x \end{bmatrix} \tag{37}$$

As so, the term $d\mathbf{A}^T\boldsymbol{\sigma}$ can be represented as,

$$d\mathbf{A}^T\,\boldsymbol{\sigma} = \begin{bmatrix} \sigma_{xx} \underset{[3\times3]}{\mathbf{I}} & \tau_{zx} \underset{[3\times3]}{\mathbf{I}} & \tau_{yz} \underset{[3\times3]}{\mathbf{I}} \\ \tau_{zx} \underset{[3\times3]}{\mathbf{I}} & \sigma_{yy} \underset{[3\times3]}{\mathbf{I}} & \tau_{xy} \underset{[3\times3]}{\mathbf{I}} \\ \tau_{yz} \underset{[3\times3]}{\mathbf{I}} & \tau_{xy} \underset{[3\times3]}{\mathbf{I}} & \sigma_{zz} \underset{[3\times3]}{\mathbf{I}} \end{bmatrix} d\boldsymbol{\theta} = \mathbf{M}\, d\boldsymbol{\theta} = \mathbf{M}\,\mathbf{G}\, d\mathbf{u} \tag{38}$$

and therefore equation (33) can be presented as,

$$\mathbf{K}_\sigma = \int_\Omega \mathbf{G}^T \, \mathbf{M} \, \mathbf{G} \, d\Omega \tag{39}$$

The initial stress matrix $\mathbf{K}_\sigma$ takes into consideration the actualized stress field.

3.2 Non-linear solution algorithms

The solution is achieved via an iterative process. In this work the iteration method used is the actualized normal plan method, considering in each new load increment the previous increment tangent stiffness matrix. Such method, which is a variant of the arc-length method, permits the solution of problems where there are the possibility of occurring structural instability, as the “snap-through” and “snap-back” phenomenon. These instability phenomenona cannot be predicted with standard nonlinear Newton-Raphson solution methods. For such nonlinear solution methods, if a control displacement analysis was used the “snap-thought” phenomenon would be solved, however the “snap-back” phenomenon would still occur.

In this work it is used the Orthogonal Actualized Ramm’s method [Crisfield M.A., (1991)], figure 3. In this method the iterative process is forced to follow an orthogonal plane to vector ${}^n\mathbf{t}^i$. For the simplicity sake the scheme of an unidimensional system solution is presented in figure 3, reducing the orthogonal plane to a bidimensional vector ${}^n\mathbf{n}^i$, where ${}^n\mathbf{n}^i \top {}^n\mathbf{t}^i$. For a given load increment n the secant vector ${}^n\mathbf{t}^i$ is obtained from,

$${}^n\mathbf{t}^i = \left({}^n\Delta\mathbf{u}^i,\ {}^n\Delta\lambda^i\mathbf{f}\right)^T \tag{40}$$

The orthogonal plane in each iteration, represented by vector ${}^n\mathbf{n}^i$, is defined by,

$${}^n\mathbf{t}^i = \left(\underbrace{{}^n\Delta\mathbf{u}^{i+1} - {}^n\Delta\mathbf{u}^i}\,{}^n d\mathbf{u}^i,\ {}^n d\lambda^i\mathbf{f}\right)^T \tag{41}$$

Since $\mathbf{t}$ and $\mathbf{n}$ are orthogonal, ${}^n\mathbf{t}^i \cdot {}^n\mathbf{n}^i = 0$, using equations (40) and (41) the value $d\lambda^i$ of can be obtained,

$$\left[{}^n\Delta\mathbf{u}^i\right]^T {}^n d\mathbf{u}^i + \left({}^n\Delta\lambda^i \cdot {}^n d\lambda^i\right)\mathbf{f}^T\mathbf{f} = \mathbf{0} \tag{42}$$

resulting after development in,

$${}^n d\lambda^i = \frac{\left[{}^n\Delta\mathbf{u}^i\right]^T {}^n\overline{d\mathbf{u}}^i}{\left[{}^n\Delta\mathbf{u}^i\right]^T {}^n d\mathbf{u}^i + \left({}^n\Delta\lambda^i\right)\mathbf{f}^T\mathbf{f}} \tag{43}$$

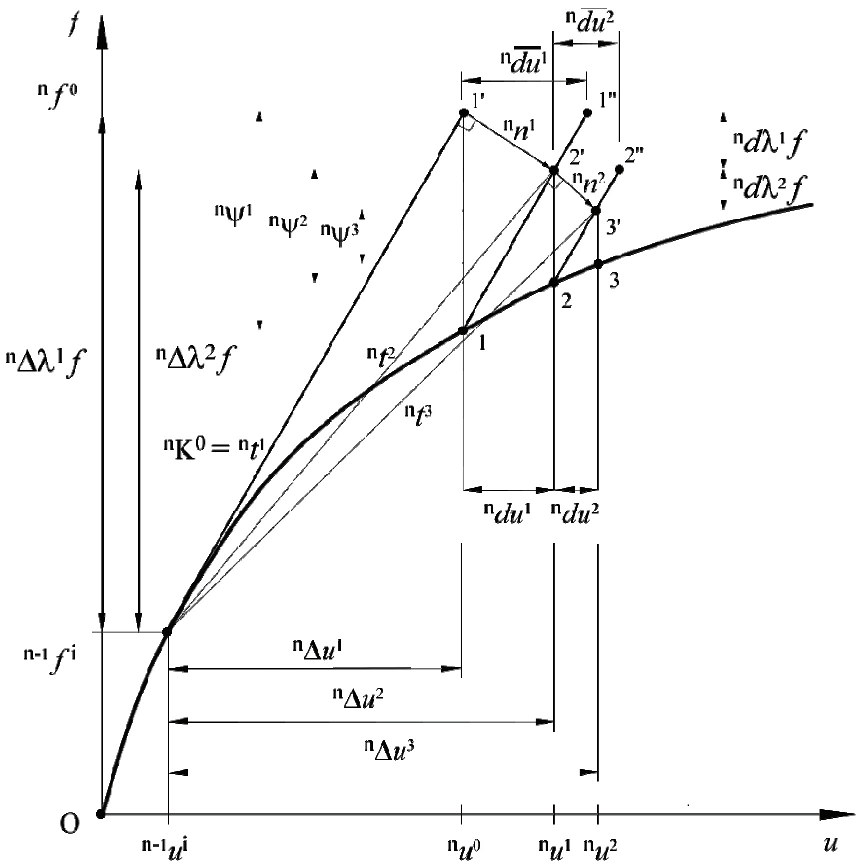

Figure 3: Orthogonal actualized Ramm's method for an unidimensional system.

In this version of the orthogonal actualized Ramm's method the tangential stiffness matrix used is determined in the first iteration of each load increment, as the Newton-Raphson method variant - Initial Increment Stiffness Method (K1) [Owen D. and Hinton E., (1980); Dinis L., Jorge R.N. et al., (2008)]. Being so, ${}^{n}d\mathbf{u}_I^i$ is constant along all the iterative process,

$$ {}^{n}d\mathbf{u}_I^i = {}^{n}\Delta\mathbf{u}^1 = \left[{}^{n}\mathbf{K}^0\right]^{-1} {}^{n}\Delta\lambda^i\mathbf{f} \tag{44} $$

The vector ${}^{n}d\bar{\mathbf{u}}^i$ can be obtained with,

$$ {}^{n}d\bar{\mathbf{u}}^i = \left[{}^{n}\mathbf{K}^0\right]^{-1} {}^{n}\psi^i \tag{45} $$

And the displacement vector in the current iteration is defined as,

$$^{n}d\mathbf{u}^{i} = \left[{}^{n}\mathbf{K}^{0}\right]^{-1\,n}\left({}^{n}\Delta\lambda^{i}\mathbf{f} - \psi^{i}\right) \tag{46}$$

The displacement vector is accumulated in each iteration,

$$^{n}\Delta\mathbf{u}^{i+1} = {}^{n}\Delta\mathbf{u}^{i} + {}^{n}d\mathbf{u}^{i} \tag{47}$$

The actualized incremental parameter is obtained with,

$$^{n}\Delta\lambda^{i+1} = {}^{n}\Delta\lambda^{i} - {}^{n}d\lambda^{i} \tag{48}$$

The generic arc-length algorithm can be summarized as in Box.1.

4 Examples

In this section several examples are presented in order to prove the high accuracy and the good behaviour of the NNRPIM. Firstly the application of the orthogonal actualized Ramm's method to the NNRPIM is validated by comparison with the Newton-Raphson non-linear solution method. Then the efficiency of the arch method applied to the NNRPIM is tested with a problem that shows structural instability. Afterwards the solutions obtained with NNRPIM for large deformation benchmark examples are presented. The NNRPIM solution is compared with analytical solution and FEM solutions, whenever available.

4.1 Clamped Thick Arch

In this example a thick arch is studied, clamped in both ends and subjected to a concentrated load in the mid span, as figure 4 shows.

The material properties of the arch are $E = 4.8MPa$ and several values for Poisson ratios are considered, $\nu = \{0.00\ 0.10\ 0.20\ 0.30\ 0.40\ 0.49\}$, these values are used along the analysis. Using the symmetry of the solid only half of the problem is studied. The problem is analysed using two distinct approaches, a 2D approach and a 3D approach. The nodal meshes used in the analysis are presented in figure 5. The NNRPIM solution is compared with the analytical solution presented in [Schreyer H.L. and Masur E.F., (1966)].

In order to study the influence of the nodal mesh discretization in the accuracy of the solution, it was considered the three regular meshes presented in figure 5(a), 5(b) and 5(c). The load applied versus the displacement along z direction in the mid-span of the arch is presented in figure 6. The non-linear solution method used to solve the large deformation problem is the initial stiffness Newton-Raphson

Box 1: Generic arc-length algorithm.

---

i. In the beginning of the load incremental process it is determined,

$$ {}^{n}\overline{d\boldsymbol{u}}^{0} = \left[{}^{n}\boldsymbol{K}^{0} \right]^{-1} \; {}^{n}\Delta\lambda^{1} \boldsymbol{f} = {}^{n}\Delta\boldsymbol{u}^{1} = {}^{n}d\boldsymbol{u}_{\mathrm{I}}^{\mathrm{i}} = {}^{n}d\boldsymbol{u}^{0} \qquad \mathrm{B.(1)} $$

note that ${}^{n}d\boldsymbol{u}_{\mathrm{I}}^{\mathrm{i}}$ is constant along all the iterative process.

---

ii. With the obtained displacement field the stress field is determined in each iteration,

$$ {}^{n}d\boldsymbol{\sigma}^{\mathrm{i}} = \boldsymbol{c} \; {}^{n}\overline{\boldsymbol{B}}^{\,\mathrm{i}} \; {}^{n}d\boldsymbol{u}^{\mathrm{i}} \qquad \mathrm{B.(2)} $$

---

iii. The residual force vector is obtained,

$$ {}^{n}\psi^{\mathrm{i}} = {}^{n}\Delta\lambda^{\mathrm{i}} \boldsymbol{f} - \int_{\Omega} {}^{n}\overline{\boldsymbol{B}}^{\,\mathrm{i}} \; {}^{n}d\boldsymbol{\sigma}^{\mathrm{i}} \; d\Omega \qquad \mathrm{B.(3)} $$

---

iv. The iterative process is concluded when a certain convergence criterion is reached, achieving the converged solution for increment n. It is used a force convergence criterion,

$$ \mathrm{e}_{\mathrm{t}} = \frac{\left\| {}^{n}\psi^{\mathrm{i}} \right\|}{\left\| {}^{n}\Delta\lambda^{\mathrm{i}} \boldsymbol{f} \right\|} \qquad \mathrm{B.(4)} $$

If $\mathrm{e}_{\mathrm{t}} \leq \mathrm{toler}$ the process stops and it moves to the next load increment $\mathrm{n}+1$. The toler parameter is a scalar within the interval $\mathrm{toler} \in \left[10^{-4}, 10^{-2} \right]$.

---

v. Else if $\mathrm{e}_{\mathrm{t}} > \mathrm{toler}$ the iteration process continues and it is determined the ${}^{n}d\lambda^{\mathrm{i}}$. First ${}^{n}\overline{d\boldsymbol{u}}^{\mathrm{i}}$ is obtained,

$$ {}^{n}\overline{d\boldsymbol{u}}^{\mathrm{i}} = \left[{}^{n}\boldsymbol{K}^{0} \right]^{-1} \; {}^{n}\psi^{\mathrm{i}} \qquad \mathrm{B.(5)} $$

and then,

$$ {}^{n}d\lambda^{\mathrm{i}} = \frac{-\left[{}^{n}\Delta\boldsymbol{u}^{\mathrm{i}} \right]^{\mathrm{T}} \; {}^{n}\overline{d\boldsymbol{u}}^{\mathrm{i}}}{\left[{}^{n}\Delta\boldsymbol{u}^{\mathrm{i}} \right]^{\mathrm{T}} \; {}^{n}d\boldsymbol{u}_{\mathrm{I}}^{\mathrm{i}} + \left({}^{n}\Delta\lambda^{\mathrm{i}} \right) \boldsymbol{f}^{\mathrm{T}} \boldsymbol{f}} \qquad \mathrm{B.(6)} $$

---

vi. The displacement vector of current iteration ${}^{n}d\boldsymbol{u}^{\mathrm{i}}$ is determined, with ${}^{n}d\boldsymbol{u}^{\mathrm{i}} = \left[{}^{n}\boldsymbol{K}^{0} \right]^{-1} \left({}^{n}\Delta\lambda^{\mathrm{i}} \boldsymbol{f} - {}^{n}\psi^{\mathrm{i}} \right)$, and accumulated ${}^{n}\Delta\boldsymbol{u}^{\mathrm{i+1}}$, with ${}^{n}\Delta\boldsymbol{u}^{\mathrm{i+1}} = {}^{n}\Delta\boldsymbol{u}^{\mathrm{i}} + {}^{n}d\boldsymbol{u}^{\mathrm{i}}$. A new load level of the next iteration is establish ${}^{n}\Delta\lambda^{\mathrm{i+1}}$, with ${}^{n}\Delta\lambda^{\mathrm{i+1}} = {}^{n}\Delta\lambda^{\mathrm{i}} - {}^{n}d\lambda^{\mathrm{i}}$.

---

vii. With the displacement vector of current iteration determined one can move to step 2, and re-start the iterative process until the convergence criterion is reached.

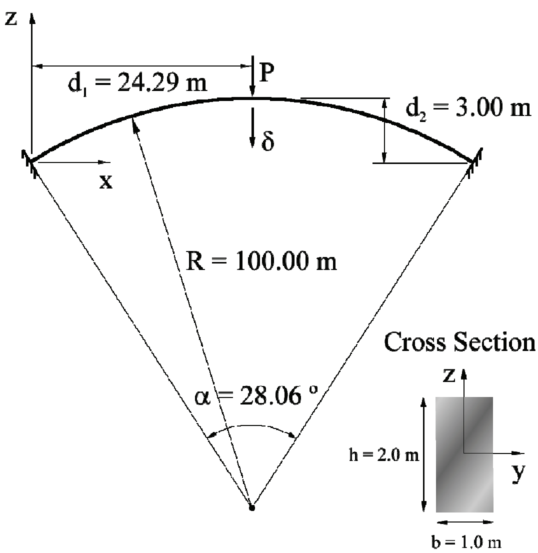

Figure 4: Geometrical model of proposed thick arch.

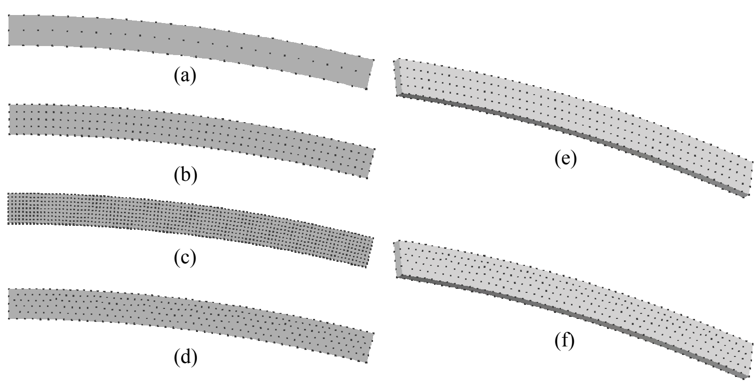

Figure 5: Meshes used in the analysis. (a) 2D regular 73 nodal mesh. (b) 2D regular 255 nodal mesh. (c) 2D regular 909 nodal mesh. (d) 2D irregular 303 nodal mesh. (e) 3D regular 510 nodal mesh. (f) 3D irregular 606 nodal mesh.

method. As figure 6 indicates the solution converges. It also shows that there is a good concordance between the analytical solution and the 2D solution obtained with the NNRPIM. The numerical implementation of the non-linear solution method (KT1) was successfully applied to the NNRPIM [Dinis L., Jorge R.N. et al.,

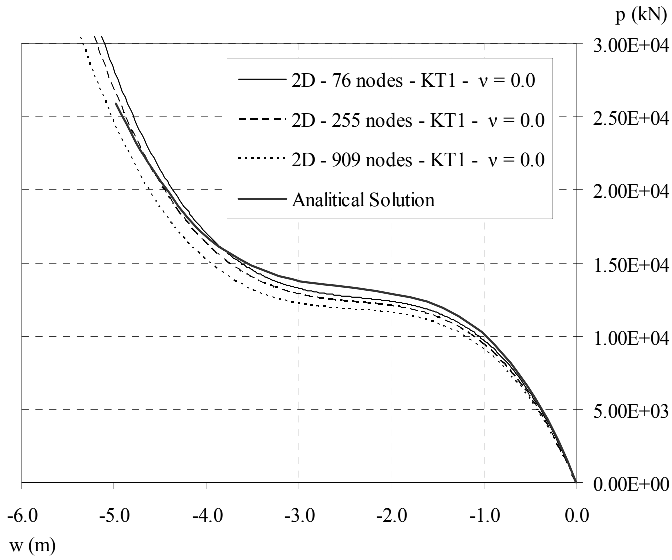

Figure 6: Evolution of the displacement on the mid span of the arch for distinct meshes.

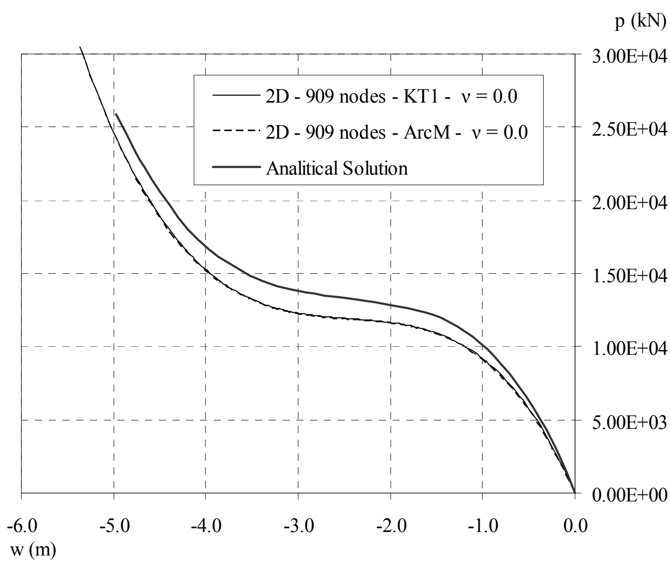

Figure 7: Evolution of the displacement on the mid span of the arch when two distinct non-linear solution methods are used.

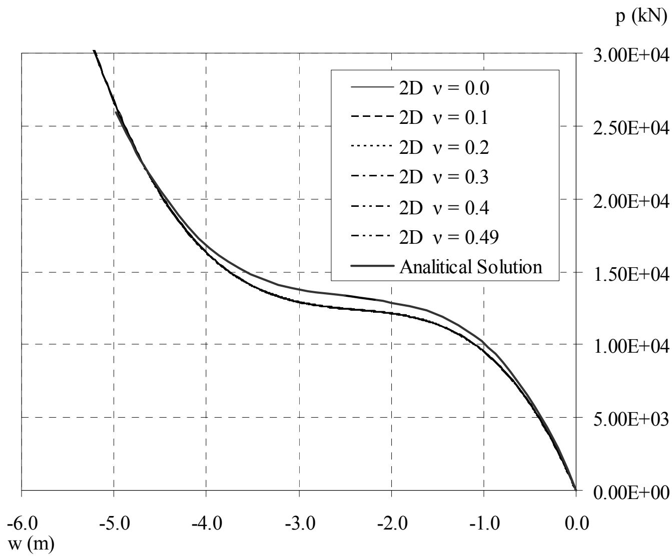

Figure 8: Evolution of the displacement on the mid span of the arch for several values of the Poisson ratio.

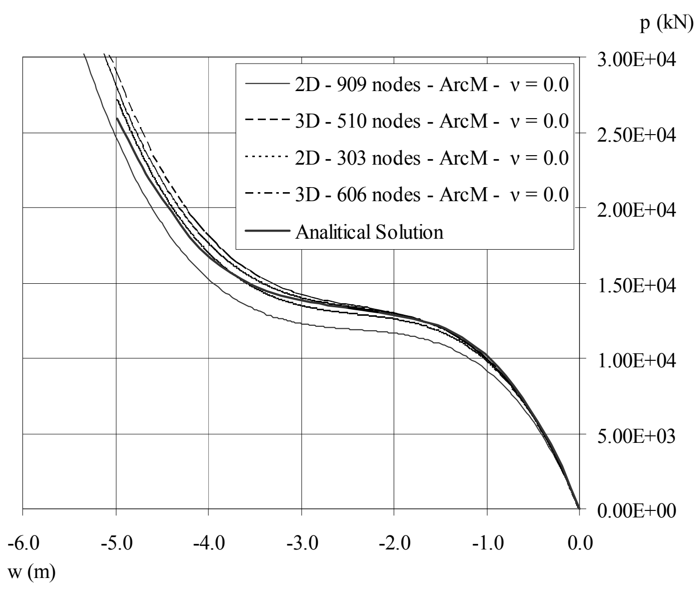

Figure 9: Evolution of the displacement on the mid span of the arch obtained with a 3D formulation and with irregular meshes.

(2008)], thus it is important to validate the orthogonal actualized Ramm's method, or arch-method, comparing the results obtained with the KT1 with the results obtained with the arch-method (ArcM). In figure 7 both non-linear solution methods are compared. As it is visible on figure 7, both non-linear solution methods produce coincident results, as it should be. As so, from this example forward, in this work all the next examples are solved using the orthogonal actualized Ramm's method.

The same problem is now considered but the Poisson ratio is varied between 0 and 0.49. The mesh used in the analysis is the 255 nodes regular mesh. The load applied versus the displacement along z direction in the mid-span of the arch is presented in figure 8. It is visible that the Poisson ratio does not significantly influence the obtained solution.

The NNRPIM 3D formulation is now applied to solve the problem. The 3D regular and irregular meshes presented respectively in figure 5(e) and 5(f) are used in the analysis. A 2D irregular mesh of 303 nodes, figure 5(d), is also used in the analysis. The results are compared with the 2D solution (909 nodes regular mesh) and the analytical solution. The results are presented in figure 9 and it is visible the good concordance between the 3D solution and the analytical solution, regardless if it is a 3D regular mesh or a 3D irregular mesh.

As figure 9 shows the irregularity of the mesh does not disturb the method performance or accuracy.

4.2 Simply Supported Shallow Arch

A clamped shallow arch which has the snap-through buckling behaviour was analyzed. The arch is loaded by a point load at the top centre and it is simply supported in both ends in the centre of the section. The geometry and dimensions are shown in Figure 10. The material properties of the arch are $E = 700MPa$ and $\nu = 0.0$. Using the symmetry of the solid only half of the problem is studied. The results are compared with a FEM solution for a 1D analysis using the Timoshenko beam element solution [Gomes C.R., (1982)].

The problem is solved considering the 2D and the 3D approach. The regular and irregular meshes, 2D and 3D, used in the analysis are shown in figure 11.

The vertical displacement on the mid span of the arch in relation to the applied load is present in figure 12. It is visible in figure 12 that the orthogonal actualized Ramm's method algorithm predicts well the snap-through buckling phenomenon. The NNRPIM 2D and 3D solutions are all very close to each other, regardless if the used mesh is regular or irregular. The NNRPIM solution is not very close with the FEM solution, probably because the FEM solution is regarding a 1D approach and the NNRPIM solution are for 2D and 3D analyses.

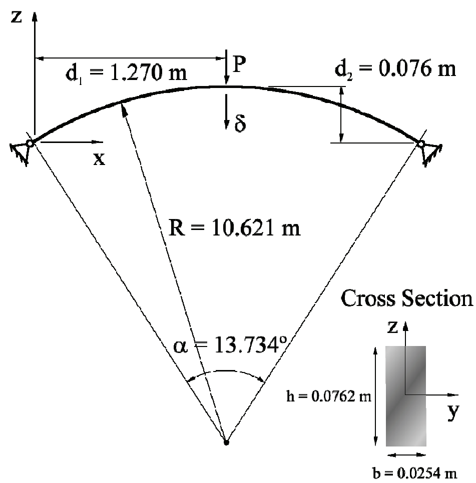

Figure 10: Geometrical model of the proposed shallow arch.

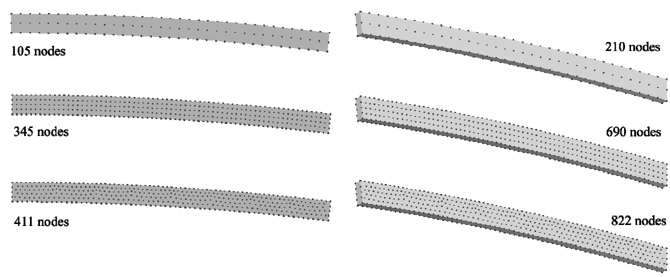

Figure 11: Meshes used in the analysis.

4.3 4.3 Pure Bending of a Cantilever Beam

Described in [Love A.E.H., (1996)] and solved numerically in several papers [Betsch P., Menzel A. et al., (1998); Areias. P.M.A., César de Sá J. M. A. et al., (2003)], this classical geometrically non-linear solid mechanics problem consists of an elastic beam subjected to a bending moment at the tip end and clamped at the other end, figure 13. The intensity of the applied moment is gradually increased until a perfect cylinder configuration is reached. The dimensions used are length $L = 10.0m$, width $B = 1.0m$ and thickness $H = 0.1m$. The Young modulus and the Poisson ratio considered are $E = 12MPa$ and $\nu = 0.0$. This problem was solved considering two distinct approaches, a 2D and a 3D approach. The 2D analysis use a regular mesh of 3×101 nodes and the 3D analysis consider a regular mesh of 126 nodes, as it is

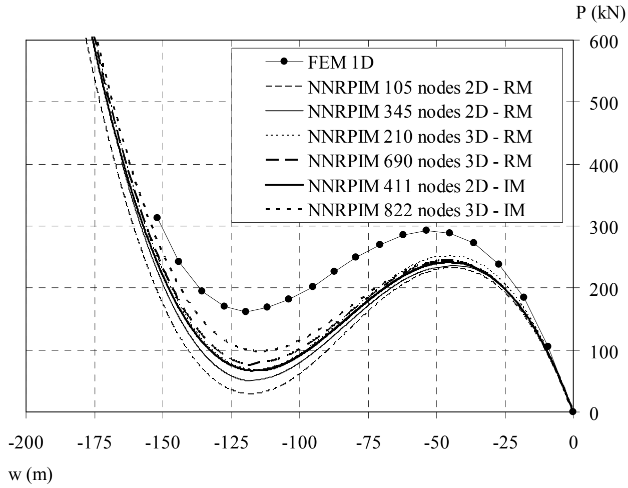

Figure 12: Displacement on the mid span of the arch.

shown in figure 13.

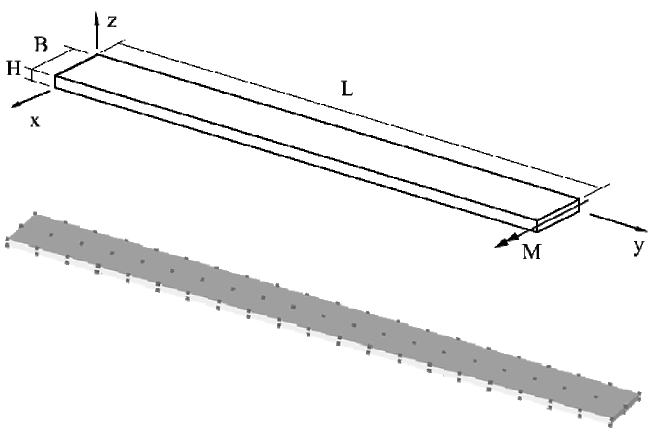

Figure 13: Geometrical model of the roll-beam proposed and Mesh used in the 3D analysis.

The numerical results obtained with the NNRPIM are presented in figure 14. Deformed meshes are presented for increasing tip moments and it is visible that the final deformed mesh is representing a nearly perfected circular ring, both for the 2D and the 3D analysis.

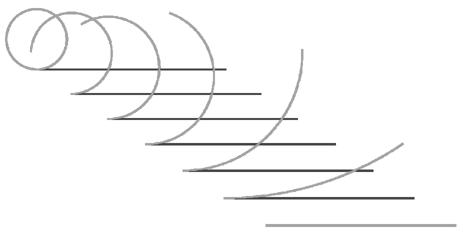

(a)

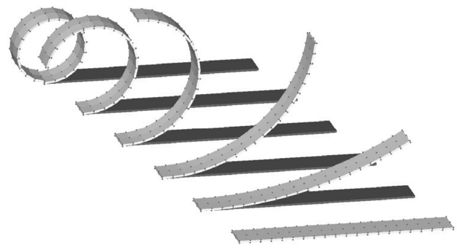

(b)

Figure 14: Deformed meshes for increasing tip moments for the 2D analysis (a) and the 3D analysis (b).

4.4 Cantilever Beam

Consider now an elastic cantilever beam with the same length $L = 10.0m$ but with a cross section $1.0 \times 1.0m^2$, the material properties are $E = 10MPa$ and $\nu = 0.3$. The load f is applied uniformly distributed at $x = L$ and the beam is clamped at $x = 0$, as figure 15 indicates. In this example two meshes for the 2D analysis and other two meshes for the 3D analysis are considered, the meshes and the number of nodes of each one are presented in figure 15.

Considering a large deformation analysis the load is applied gradually. The results obtained with the NNPRIM, for the 2D and the 3D analysis, are compared with a theoretical solution which relies on inextensional elastica [Frisch-Fay R., (1962)]. The point A, 5, displacement in the z direction of is presented in figure 16 for the several meshes considered. As it is visible on figure 16 when the mesh is refined the solution approaches the theoretical solution, for the NNRPIM-2D analysis and the NNRPIM-3D analysis. Both 2D solution and 3D solution are very near the theoretical solution. In figure 17 are presented the 2D and the 3D deformation of the cantilever beam for several increasing load levels.

As it is visible on figure 17 the displacement is smooth and there is no distortion on the mesh for largest deformations.

4.5 Square Plate Simply supported

In this example is considered a square plate subjected to a uniformly distributed load, as figure 18 indicates, where $L = D = 10.0m$ and $H = 0.5m$. The plate is simply supported in all edges for $z = 0$. Using the natural symmetry of the solid only a quarter of the plate is analysed. The considered material properties are, $E =$

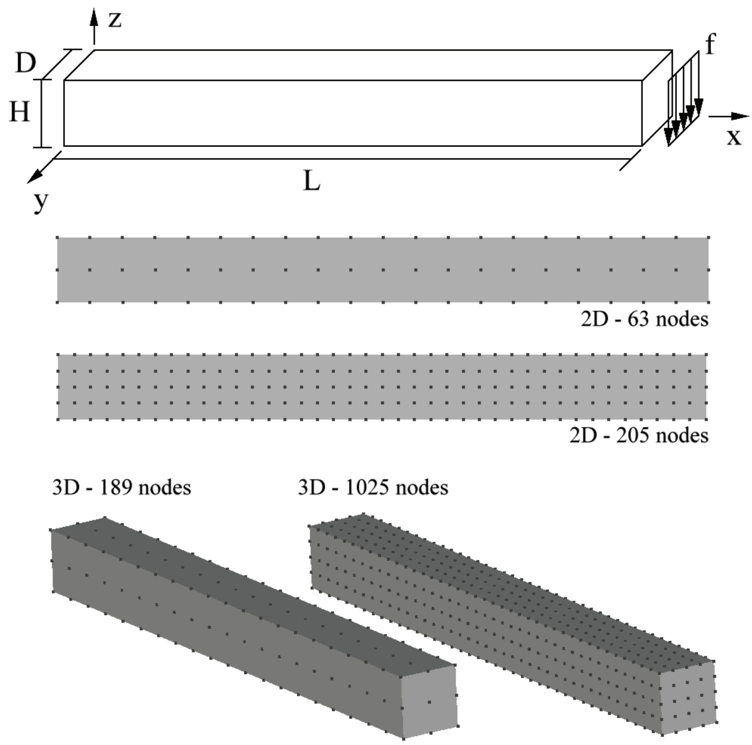

Figure 15: Geometrical model of the cantilever beam proposed and meshes considered in the analysis.

$1000kPa$ and $\nu = 0.316$. The bending of the plate is analysed using the NNRPIM 3D formulation and the results are compared with the analytical solution presented in [Chia C.Y., (1980)]. The quarter of the plate is discretized in two distinct meshes, figure 18, a regular mesh with 363 nodes and in an irregular mesh with 474 nodes are used in the 3D NNRPIM formulation, considering large deformations analysis.

In figure 19 it is presented the deformation of the plate for distinct load levels and it is perceptible the good behaviour of the NNRPIM for high levels of the applied load.

In figure 20 it is represented the displacement along the z direction on the centre of the plate for increasing load levels. The NNRPIM results are close to the analytical solution, regardless if a regular or an irregular mesh is used in the analysis.

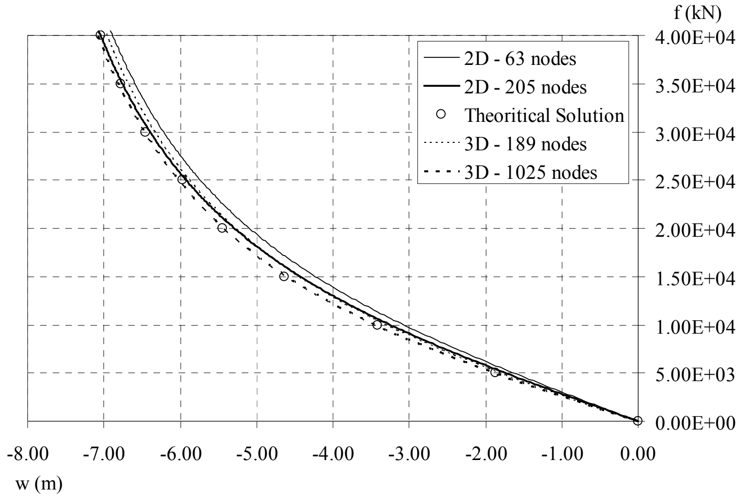

Figure 16: Evolution of the displacement on point A with the load level for distinct meshes, for the 2D and the 3D analysis.

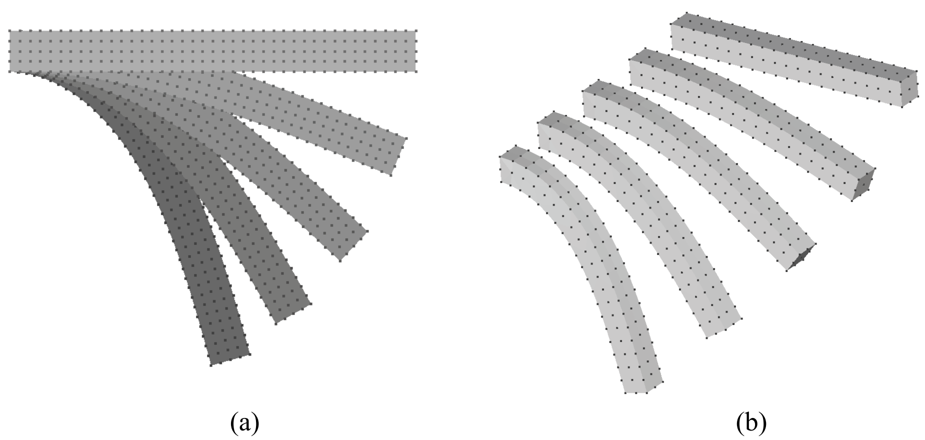

Figure 17: Deformation of the cantilever beam for several increasing load levels for the 2D analysis (a) and 3D analysis (b).

4.6 Clamped Square Plate

In this example a square plate clamped in all edges is analysed. The material and geometrical properties, along with the load condition, are the same of the pervious example. Also the two distinct meshes presented in figure 18(b) and 18(c) are used, the 363 node regular mesh and the 474 node irregular mesh. The results obtained

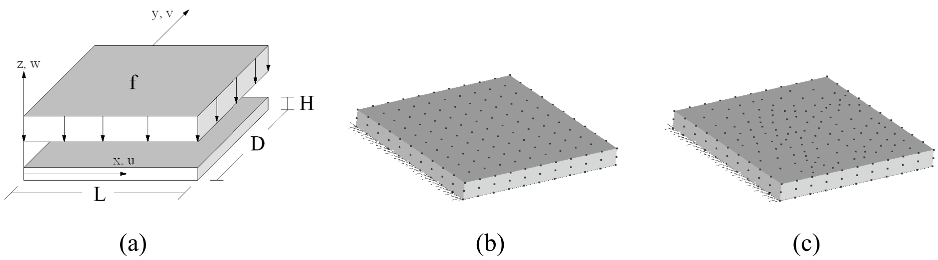

Figure 18: (a) Geometrical model of the plate and applied load. (b) Regular mesh with 363 nodes and (c) Irregular mesh with 474 nodes.

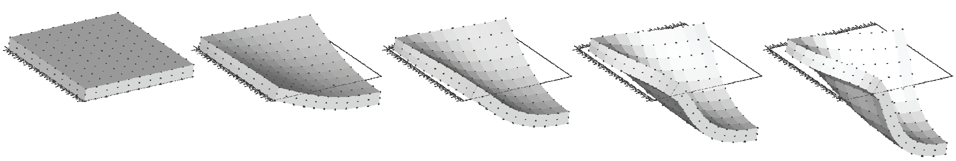

Figure 19: Deformation of the simply supported square plate for several increasing load levels.

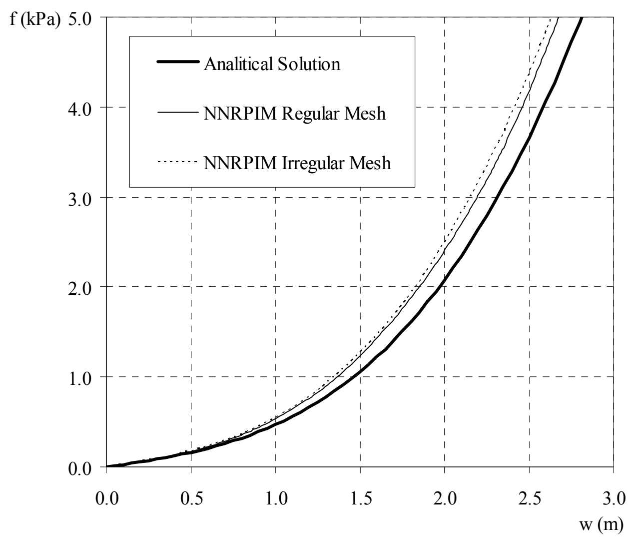

Figure 20: Evolution of the central displacement of the plate with the load level, for the 3D analysis.

applying the NNRPIM 3D formulation and using large deformation analysis are compared with the analytical solution presented in [Chia C.Y., (1980)]. One again the good behaviour of the NNRPIM is shown in figure 21. The 3D displacement field obtained in the analysis, for distinct load levels, is always smooth and accurate.

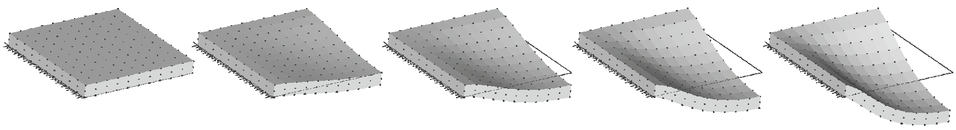

Figure 21: Deformation of the clamped square plate for several increasing load levels.

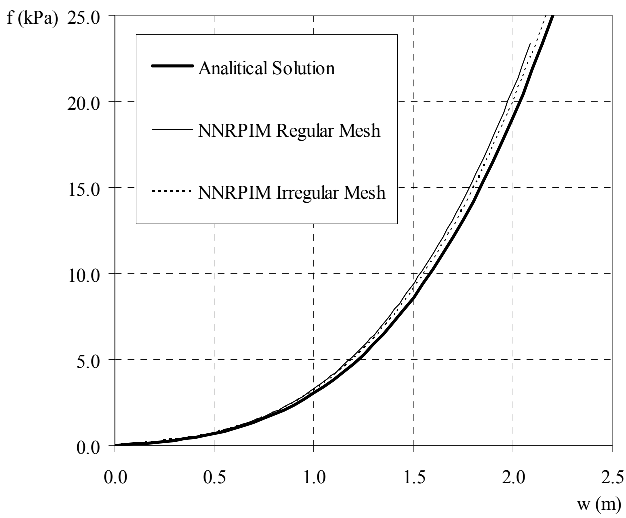

Figure 22: Central displacement of the plate in relation to the applied load for the 3D analysis.

The displacement along the z direction on the centre of the plate for increasing load levels is presented in figure 22. It is perceptible that the NNRPIM solution is almost coincident with the analytical solution.

4.7 Curved Cantilever Beam

The following example shows the applicability of the NNRPIM for thin 3-D-beams. The large displacement response of a three-dimensional curvilinear cantilever beam subject to a concentrated end load is calculated [Bathe K.J. and Bolourchi S., (1979)]. Due to the geometry and the applied load the curved cantilever beam undertakes both bending and twisting deformations. The beam lies in the XY plate and its cross-sectional area is $0.01 \times 0.01 m^2$. The cantilever beam has a radius of $R = 1.0m$ and a angle on the XY plane of 45°, as figure 23 indicates. The con-

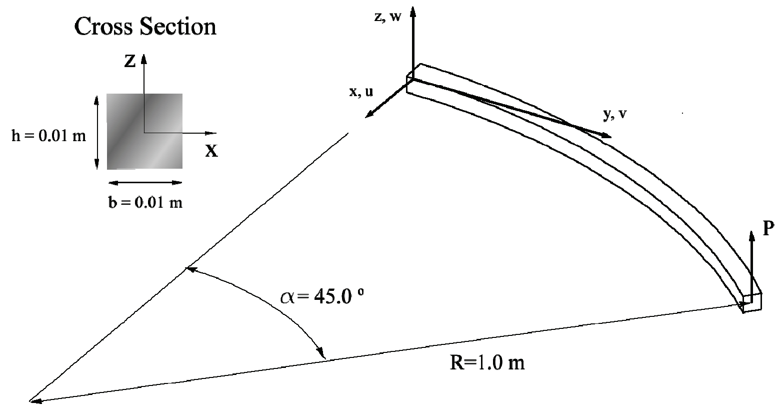

Figure 23: (a) Geometrical model of the curved cantilever beam and applied load.

centrated load is applied at one end of the beam and the opposite end is kept fixed. The analysis is carried using a Young's modulus of $E = 10MPa$ and a Poisson ratio of $\nu = 0.0$. Several three-dimensional meshes are used in the analysis, as figure 24 shows. The NNRPIM results are compared with an optimized FEM solution [Bathe K.J. and Bolourchi S., (1979)].

The NNRPIM results for the end tip of the curve beam, regarding the three variables of the displacement, are presented in figures 25, 26 and 27. The applied load is normalized with the expression $P_{norm} = P \times R^2/(E \times I)$ being I the inertia of the beam cross section. As it is visible, there is a path of convergence for the NNRPIM. With the refinement of the mesh the NNRPIM solution approaches the reference FEM solution. Using mesh 5, the most refine mesh, the results approach more the FEM solution.

In figure 28 it is presented the deformation of the curved beam for distinct load levels and it is perceptible the good behaviour of the NNRPIM for high levels of the applied load.

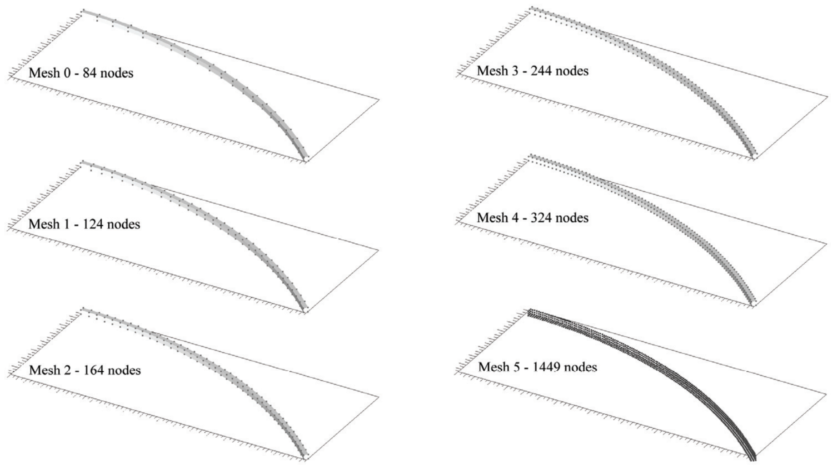

Figure 24: Meshes used in the analysis.

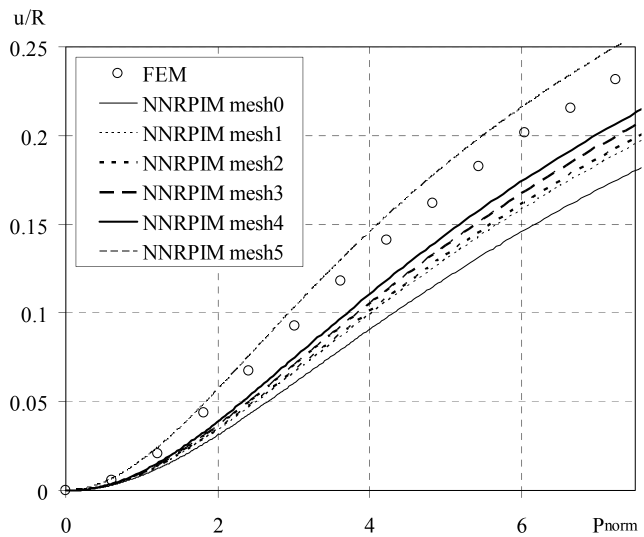

Figure 25: Evolution of the displacement along x direction on the end tip of the curved cantilever beam with the load level, for distinct meshes.

5 Conclusions

In this work the Natural Neighbour Radial Point Interpolation Method (NNRPIM) was extended to the large deformation analysis of non-linear elastic structures. The

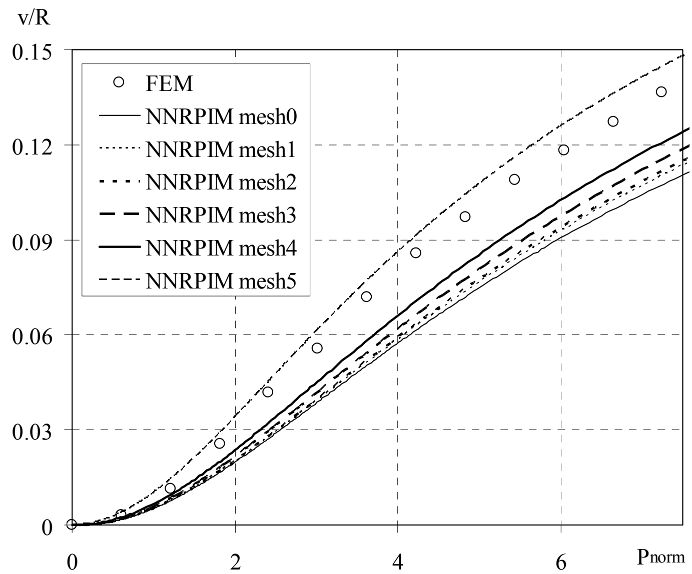

Figure 26: Evolution of the displacement along y direction on the end tip of the curved cantilever beam with the load level, for distinct meshes.

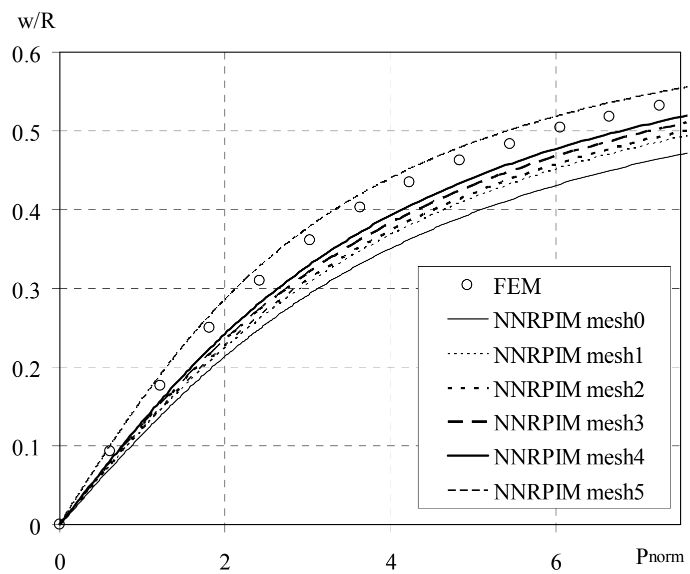

Figure 27: Evolution of the displacement along z direction on the end tip of the curved cantilever beam with the load level, for distinct meshes.

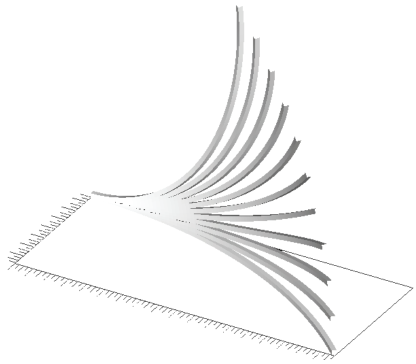

Figure 28: Deformation of the curved beam for several increasing load levels.

Orthogonal Actualized Ramm's method was used for the solution of the nonlinear system of equations. From the experience acquired along the development of this work along with the results obtained with the presented benchmark examples, it can be concluded,

1. The NNRPIM is a stable and accurate interpolator meshless method. The produced displacement field and stress field is smooth, accurate and very close with the compared solutions.

2. The interpolation functions of the NNRPIM, which are very simple to construct, permit an easy imposition of the boundary conditions, reducing the computational time when compared with the approximation methods.

3. The non-linear solution algorithm, Orthogonal Actualized Ramm's method, was successfully implemented.

4. The mesh irregularity does not significantly affect the final results and the convex boundaries of the problem, due to the NNRPIM node connectivity scheme, does not represent a setback, as in other meshless methods that use the influence domain concept.

The NNRPIM proved to be an alternative method in the large deformation analysis of non-linear elastic structures.

Acknowledgement: The authors truly acknowledge the funding provided by Ministério da Ciência, Tecnologia e Ensino Superior – Fundação para a Ciência e a

Tecnologia (Portugal), under grant SFRH/BD/31121/2006, and by FEDER/FSE, under grant PTDC/EME-PME/81229/2006.

References

.**Areias. P.M.A., César de Sá J. M. A., Conceicao Antonio C. A., Fernandes A.A.** (2003): Analysis of 3D problems using a new enhanced strain hexahedral element. *International Journal for Numerical Methods in Engineering* vol 58: 1637–1682.

Atluri S.N., Han Z.D., Rajendran A.M. (2004): A New Implementation of the Meshless Finite Volume Method, Through the MLPG "Mixed" Approach. *CMES: Computer Modeling in Engineering & Sciences* vol 6(6): 491-514.

Atluri S.N., Shen S. (2002): The Meshless Local Petrov-Galerkin (MLPG) Method: A Simple and Less-costly Alternative to the Finite Element and Boundary Element Methods. *CMES: Computer Modeling in Engineering & Sciences* vol 3(1): 11-52.

Atluri S.N., Zhu T. (1998): A new meshless local Petrov-Galerkin (MLPG) approach in computational mechanics. *Computational Mechanics* vol 22(2): 117-127.

Bardenhagen S.G., Kober E.M. (2004): The Generalized Interpolation Material Point Method. *CMES: Computer Modeling in Engineering & Sciences* vol 5(6): 477-496.

Bathe K.J., Bolourchi S. (1979): Large displacement analysis of three-dimensional beam structures. *International Journal for Numerical Methods in Engineering* vol 14: 961-986.

Belytschko T., Krongauz Y., Organ D., Fleming M., Krysl P. (1996): Meshless Methods: an overview and recent developments. *Computer Methods in Applied Mechanics and Engineering* vol 139(1): 3-47.

Belytschko T., Lu Y.Y., Gu L. (1994): Element-Free Galerkin Method. *International Journal for Numerical Methods in Engineering* vol 37: 229-256.

Betsch P., Menzel A., Stein E. (1998): On parametrization of finite rotations in computational mechanics. A classification of concepts with application to smooth shells. *Computer Methods in Applied Mechanics and Engineering* vol 155: 273–305.

Braun J., Sambridge M. (1995): A numerical method for solving partial differential equations on highly irregular evolving grids. *Nature* vol 376: 655-660.

Chia C.Y. (1980): Non Linear Analysis of Plates, McGraw-Hill.

Crisfield M.A. (1991): Non-Linear Finite Element Analysis of Solids and Structures, Jonh Wiley and Sons, Ltd, Baffins Lane.

Cueto E., Doblare M., Gracia L. (2000): Imposing essential boundary conditions in the natural element method by means of density-scaled -shapes. *International Journal for Numerical Methods in Engineering* vol 49(4): 519-546.

Cueto E., Sukumar N., Calvo B., Cegonino J., Doblare M. (2003): Overview and recent advances in the Natural Neighbour Galerkin Method. *Archives of Computational Methods in Engineering* vol 10(4): 307-387.

Delaunay B. (1934): Sur la sphere vide. A la memoire de Georges VoronoÃ¯. *Izv. Akad. Nauk SSSR, Otdelenie Matematicheskih i Estestvennyh Nauk* vol 7: 793-800.

Devi K.N., Pepper D.W. (2004): A Meshless Radial Basis Function Method for Fluid Flow with Heat Transfer. *CMES: Computer Modeling in Engineering & Sciences* vol 6(1): 13-18.

Dinis L., Jorge R.N., Belinha J. (2007a). Analysis of 3D solids using the natural neighbour radial point interpolation method. *Computer Methods in Applied Mechanics and Engineering* vol 196: 2009-2028.

Dinis L., Jorge R.N., Belinha J. (2007b). Analysis of plates and laminates using the natural neighbour radial point interpolation method. *Engineering Analysis with Boundary Elements* vol 32: 267-279.

Dinis L., Jorge R.N., Belinha J. (2008): Radial Natural Neighbours Interpolators: 2D and 3D Elastic and Elastoplastic Applications. *Progress on Meshless Methods*. Ferreira A.J.M., Kansa E.J., Fasshauer G.E. and Leitao V.M.A., Springer. vol 11.

Frisch-Fay R. (1962): Flexible Bars, Butterworths, London.

Gomes C.R. (1982): Matrix Update Methods in Nonlinear Analysis of two Dimensional and thin Shell Problems. Civil Engineering. *Swansea*, University of Wales.

Gu Y.T. (2005): Meshfree methods and their comparisons. *International Journal of Computational Methods* vol 2(4): 477-515.

Han Z.D., Rajendran A.M., Atluri S.N (2005): Meshless Local Petrov-Galerkin (MLPG) Approaches for Solving Nonlinear Problems with Large Deformations and Rotations. *CMES: Computer Modeling in Engineering & Sciences* vol 10(1): 1-12.

Hardy R.L. (1990): Theory and applications of the multiquadrics - Biharmonic method (20 years of discovery 1968-1988). *Computers and Mathematics with Applications* vol 19: 127-161.

Juan Z., Shuyao L., Yuanbo X., Guangyao L. (2008): A Topology Optimization Design for the Continuum Structure Based on the Meshless Numerical Technique. *CMES: Computer Modeling in Engineering & Sciences* vol 34(2): 137-154.

Kansa E.J. (1990): A scattered data approximation scheme with applications to computational fluid-dynamics - I & II. *Computers and Mathematics with Applications* vol 19: 127-161.

Lancaster P., Salkauskas K. (1981): Surfaces Generation by Moving Least Squares Methods. *Mathematics of Computation* vol 37: 141-158.

Leevan Ling (2005): Meshless Unsymmetric CollocationMethod. *CMES: Computer Modeling in Engineering & Sciences* vol 8(4): 133-137.

Liu G.R. (2002a). Mesh Free Methods, Moving beyond the Finite Element Method, CRC Press.

Liu G.R. (2002b). A Point Assembly Method for Stress Analysis for Two-Dimensional Solids. *International Journal of Solid and Structures* vol 39: 261-276.

Liu G.R., Gu Y.T. (2001): A Point Interpolation Method for Two-Dimensional Solids. *International Journal for Numerical Methods in Engineering* vol 50: 937-951.

Liu G.R., Gu Y.T., Dai K.Y. (2004): Assessment and applications of interpolation methods for computational mechanics. *International Journal for Numerical Methods in Engineering* vol 59: 1373-1379.

Liu W.K., Jun S., Zhang Y.F. (1995): Reproducing Kernel Particle Methods. *International Journal for Numerical Methods in Fluids* vol 20(6): 1081-1106.

Liu Y.H., Chen S.S., Li J., Cen Z.Z. (2008): A Meshless Local Natural Neighbour Interpolation Method Applied to Structural Dynamic Analysis. *CMES: Computer Modeling in Engineering & Sciences* vol 31(3): 145-156.

Long S., Atluri S.N (2002): A Meshless Local Petrov-Galerkin Method for Solving the Bending Problem of a Thin Plate. *CMES: Computer Modeling in Engineering & Sciences* vol 3(1): 53-64.

Love A.E.H. (1996): A Treatise on the Mathematical Theory of Elasticity, Dover Publications: New York.

Lu Y., Belytschko T., Gu L. (1994): A New Implementation of the Element Free Galerkin Method. *Computer Methods in Applied Mechanics and Engineering* vol 113: 397-414.

Ma J., Lu H., Komanduri R. (2006): Structured Mesh Refinement in Generalized Interpolation Material Point (GIMP) Method for Simulation of Dynamic Problems. *CMES: Computer Modeling in Engineering & Sciences* vol 12(3): 213-228.

Mohammadi M.H. (2008): Stabilized Meshless Local Petrov-Galerkin (MLPG) Method for Incompressible Viscous Fluid Flows. *CMES: Computer Modeling in Engineering & Sciences* vol 29(2): 75-94.

Monaghan J.J. (1977): Smoothed Particle Hydrodynamics: Theory and Applications to Non-Spherical Stars. *Monthly Notices of the Astronomical Society* vol 181: 375-389.

Nayroles B., Touzot G., Villon P. (1992): Generalizing the Finite Element Method: Diffuse Approximation and Diffuse Elements. *Computational Mechanics* vol 10: 307-318.

Owen D., Hinton E. (1980): Finite Element in Plasticity, Pineridge press.

Qian L.F., Batra R.C., Chen L.M. (2003): Free and Forced Vibrations of Thick Rectangular Plates using Higher-Order Shear and Normal Deformable Plate Theory and Meshless Petrov-Galerkin (MLPG) Method. *CMES: Computer Modeling in Engineering & Sciences* vol 4(5): 519-534.

Schreyer H.L., Masur E.F. (1966): Buckling of shallow arches. *ASCE Journal of Engineering Mechanics Division* vol EM4: 1–19.

Sibson R. (1980): A vector identity for the Dirichlet tesselation. *Mathematical Proceedings of the Cambridge Philosophical Society* vol 87: 151-155.

Sladek V., Sladek J., Zhang C. (2003): A Comparative Study of Meshless Approximations in Local Integral Equation Method. *CMES: Computer Modeling in Engineering & Sciences* vol 4(3): 177-188.

Sori J., Q. Li Q., Jarak T., Atluri S.N (2004): Meshless Local Petrov-Galerkin (MLPG) Formulation for Analysis of Thick Plates. *CMES: Computer Modeling in Engineering & Sciences* vol 6(4): 349-358.

Sukumar N., Moran B., Belytschko T. (1998): The natural element method in solid mechanics. *International Journal for Numerical Methods in Engineering* vol 43(5): 839–887.

Sukumar N., Moran B., Semenov A.Y., Belikov V.V. (2001): Natural neighbour Galerkin methods. *International Journal for Numerical Methods in Engineering* vol 50(1): 1-27.

Traversoni L. (1994): Natural Neighbour Finite Elements. *Int. Conf. on Hydraulic Engineering Software, Hydrosoft Proc., Computational Mechanics Publications* vol 2: 291-297.

Vavourakis V., Sellountos E.J., Polyzos D. (2006): A comparison study on different MLPG (LBIE) formulations. *CMES: Computer Modeling in Engineering & Sciences* vol 13(3): 171-184.

Voronoį G.M. (1908): Nouvelles applications des parametres continus Ã la thÃ©orie des formes quadratiques. *Deuxieme Memoire: Recherches sur les parallelloedres primitifs, J. Reine Angew. Math.* vol 134: 198-287.

Wang J.G., Liu G.R. (2002a): On the Optimal Shape Parameters of Radial Basis Functions used for 2-D Meshless Methods. *Computer Methods in Applied Mechan-*

ics and Engineering vol 191: 2611-2630.

Wang J.G., Liu G.R. (2002b): A Point Interpolation Meshless Method based on Radial Basis Functions. *International Journal for Numerical Methods in Engineering* vol 54: 1623-1648.

Wen P.H., Hon Y.C. (2007): Geometrically Nonlinear Analysis of Reissner-Mindlin Plate by Meshless Computation. *CMES: Computer Modeling in Engineering & Sciences* vol 21(3): 177-192.